Journal of Materials Chemistry C

ROYAL SOCIETY OF CHEMISTRY

PAPER

View Article Online
View Journal | View Issue

Check for updates

Cite this: J. Mater. Chem. C, 2022, 10, 2792

An asymmetric A–DA′D–π-A type non-fullerene acceptor for high-performance organic solar cells†

Zhe Zhang,‡[a] Dawei Li,‡[a] Huarui Zhang,[b] Xueqin Ma,[b] Ya-Nan Chen,[c] Andong Zhang,[c] Xiaoyun Xu,[d] Yahui Liu,*[c] Zaifei Ma [d] and Zhishan Bo *[bc]

Received 15th September 2021,
Accepted 11th November 2021

DOI: 10.1039/d1tc04425g

rsc.li/materials-c

Under the guidance of a symmetry-breaking and π-bridge-extending strategy, three asymmetric and symmetric non-fullerene acceptors (**L1**, **L2**, and **L3**) with DA′D core units and two 2-(5,6-difluoro-3-oxo-2,3-dihydro-1*H*-inden-1-ylidene)malononitrile electron-withdrawing units (A) have been designed and synthesized *via* changing the alkoxy-substituted thiophene bridge unit. The asymmetric A–DA′D–π-A-type non-fullerene acceptor (NFA) **L2** displays much improved solubility and a slightly larger molar absorption coefficient than its symmetric counterparts (**L1** and **L3**). In addition, blend film based on the asymmetric NFA **L2** shows suitable nanoscale phase morphology and much higher and more balanced hole and electron mobilities. Hence, compared with **L1**- and **L3**-based organic solar cells (OSCs), optimal **L2**-based devices can deliver a high power-conversion efficiency (PCE) of 14.06% with simultaneously enhanced current density and fill factor values. Our study indicates that a combined symmetry-breaking and π-bridge-extending strategy is powerful for the design of high-performance NFAs.

Published on 17 novembra 2021. Downloaded on 13.10.2025 2:24:29.

Introduction

Organic solar cells (OSCs) have attracted much attention during the past several years due to their intrinsic advantages, such as being lightweight and flexible, having roll-to-roll processing capacity, *etc.*[1–6] In the past several decades, fullerene-derivative acceptors have become prevalent in the field of OSCs. However, the inherent drawbacks of fullerene derivatives, such as their narrow and weak absorption, nonadjustable energy levels, poor stability, *etc.*, have limited further improvements in the photovoltaic performances of OSCs. By 2016, the power conversion efficiencies (PCEs) of OSCs had reached a bottleneck of approximately 11%. However, in recent years, researchers have focused on alternative acceptors, so-called non-fullerene acceptors (NFAs), promoting the rapid development of OSCs. Nowadays, the PCEs of single-junction OSCs have reached over 18%,[7,8] demonstrating great potential for commercial applications.

Typical high-performance NFAs have A–D–A-type molecular configurations, which usually consist of three parts:[9–12] a large planar electron-donating multi-fused-ring core unit (D); electron-withdrawing terminal groups (A); and out-of-plane side chains. The insertion of a π-bridge unit between the D and A units is a possible way to reduce the size of the central core unit. The introduction of a π-bridge unit has many advantages, such as reducing the synthetic complexity, adjusting the molecular planarity, regulating the crystallinity of acceptors, facilitating π-electron delocalization, enhancing the charge transport capacity, and, finally, improving the photovoltaic performance. A large number of high-performance A–π-D–π-A acceptors have been reported.[13–15]

Recently, Zou *et al.* reported a series of high-performance NFAs with A–DA′D–A-type molecular structures, termed Y-series acceptors.[16] These acceptors further promoted the photovoltaic performances of OSCs. Compared with typical A–D–A-type acceptors (like ITIC and IT-4F), the fused DA′D central core with two pyrrole rings and "V"-shaped molecular geometry leads to Y-series acceptors with more π–π stacking possibilities, stronger near-infrared absorption, and larger photoluminescence quantum yields.[10,17–20]

Since we reported the first fused-ring acceptors with asymmetric side chains, symmetry-breaking strategies have drawn a

[a] Key Laboratory of Eco-functional Polymer Materials of the Ministry of Education, Key Laboratory of Eco-environmental Polymer Materials of Gansu Province, College of Chemistry and Chemical Engineering, Northwest Normal University, Lanzhou 730070, China
[b] Beijing Key Laboratory of Energy Conversion and Storage Materials, College of Chemistry, Beijing Normal University, Beijing 100875, China. E-mail: zsbo@bnu.edu.cn
[c] College of Textiles & Clothing, Qingdao University, Qingdao 266071, China. E-mail: liuyh@qdu.edu.cn
[d] Center for Advanced Low-Dimension Materials, State Key Laboratory for Modification of Chemical Fibers and Polymer Materials, College of Materials Science and Engineering, Donghua University, Shanghai 201620, China

† Electronic supplementary information (ESI) available. See DOI: 10.1039/d1tc04425g

‡ These authors contributed equally to this work.

This journal is © The Royal Society of Chemistry 2022

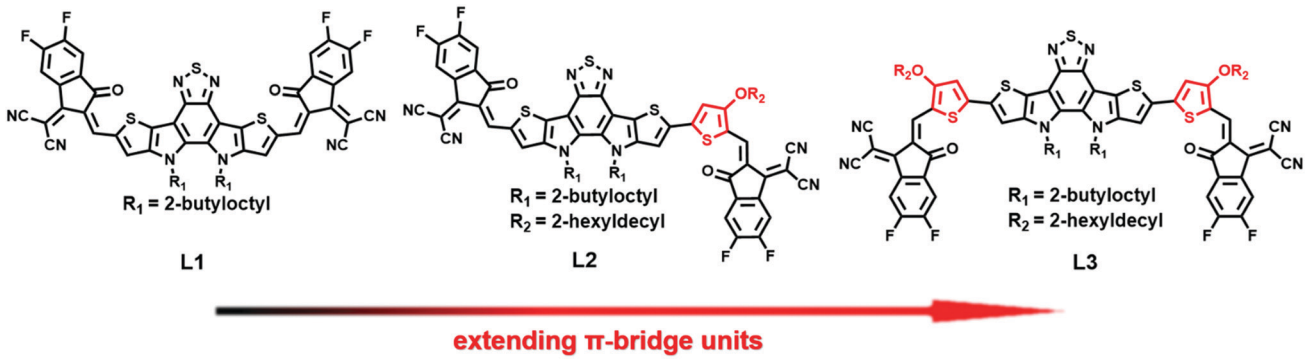

Chart 1 The chemical structures of **L1**, **L2**, and **L3**.

Published on 17 novembra 2021. Downloaded on 13.10.2025 2:24:29.

lot of attention in the design of fused-ring acceptors.[21] Various asymmetric acceptors with asymmetric core units, asymmetric side chains, and asymmetric terminal groups have been developed. Asymmetric molecular design can regulate the dipole moment, solubility, electron mobility, absorption spectrum, crystallization behaviour, *etc.*[22–28] State-of-the-art devices based on asymmetric acceptors have achieved power conversion efficiencies (PCEs) of over 17%.[29–31] However, integrated investigations involving symmetry breaking, π-bridge extension, and A–DA′D–A structures are still rare.[32]

Inspired by the above-mentioned knowledge, symmetric and asymmetric NFAs (**L1**, **L2**, and **L3**), as shown in Chart 1, with DA′D cores and 2-(5,6-difluoro-3-oxo-2,3-dihydro-1*H*-inden-1-ylidene)malononitrile electron-withdrawing units (A) are designed and synthesized *via* regulating the alkoxy-substituted thiophene bridge unit. Unexpectedly, the asymmetric acceptor **L2** displays much higher solubility than the two symmetric acceptors (**L1** and **L3**). The molar absorption coefficient of **L2** is also slightly larger than those of **L1** and **L3**. Unlike **L3**, which adopts a dominant edge-on molecular orientation, **L2** has a dominant face-on molecular orientation in neat film. As expected, **L2**-based blend film exhibits appropriate nanoscale phase separation, with high and balanced hole and electron mobilities. By comparison, **L1**-based blend film displays very low hole and electron mobilities, and **L3**-based blend film exhibits very large phase separation. Finally, OSCs based on the asymmetric acceptor **L2** can deliver an excellent PCE of 14.06%, with a high short-circuit current (J_{sc}) of 24.01 mA cm^{-2} and a fill factor (FF) of 71.73%, much higher than the PCEs of OSCs based on the symmetric acceptors **L1** (2.07%) and **L3** (1.78%). With a combination of symmetry breaking, π-bridge extension, and the use of an A–DA′D–A structure, our results provide a new molecular design strategy for high-performance NFAs.

Results and discussion

The chemical structures of **L1**, **L2**, and **L3** are shown in Chart 1, the synthetic routes to **L2** and **L3** are described in Scheme 1, and detailed procedures are provided in the ESI.† The starting material (compound **1**) and small molecule acceptor (**L1**) were prepared based on the previous literature.[33] The bromination of compound **1** with NBS gave a mixture of compounds **2** and **3**, which can be used for the next step without purification. Stille coupling of this mixture (**2** and **3**) and (4-((2-hexyldecyl)-oxy)thiophen-2-yl)trimethylstannane with $Pd(PPh_3)_4$ as the catalyst precursor afforded a mixture of intermediates (**4** and **5**).[34] Subsequently, the Vilsmeier–Haack reaction was employed to furnish compounds **6** and **7**, which can be easily separated *via* column chromatography. The target acceptors (**L2** and **L3**) were synthesized *via* the Knoevenagel condensation of the dialdehyde intermediates (**6** and **7**) with 2-(5,6-difluoro-3-oxo-2,3-dihydro-1*H*-inden-1-ylidene)malononitrile, resulting in yields of 70% and 60%, respectively. ^{1}H- and ^{13}C-NMR spectroscopy

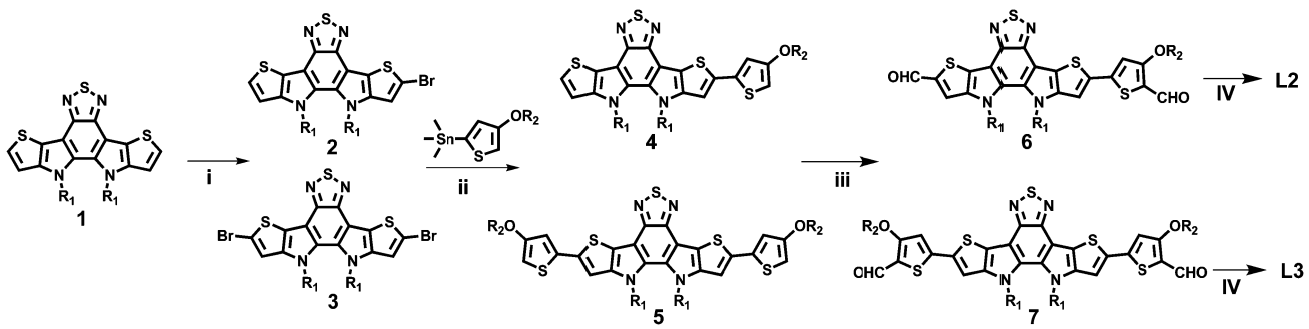

Scheme 1 Synthetic routes to **L2** and **L3**. (i) NBS, THF, 0 °C; (ii) (4-((2-hexyldecyl)oxy)thiophen-2-yl)trimethylstannane, $Pd(PPh_3)_4$, toluene, reflux; (iii) $POCl_3$, 1,2-dichloroethane, DMF, 80 °C; (iv) 2-(5,6-difluoro-3-oxo-2,3-dihydro-1*H*-inden-1-ylidene)malononitrile, pyridine, $CHCl_3$, rt.

Published on 17 novembra 2021. Downloaded on 13.10.2025 2:24:29.

and high-resolution mass spectrometry were used to verify the chemical structures of these acceptors. Furthermore, the solubilities of **L1**, **L2**, and **L3** in chlorobenzene were estimated to be 20.50, 52.90, and 13.84 mg mL^{-1}, respectively. Obviously, the asymmetric acceptor (**L2**) displays much better solubility than its symmetric counterparts (**L1** and **L3**). It is well known that good solubility is favourable for achieving better active layer morphology when blending with a donor polymer.

The UV-vis absorption behaviours of **L1**, **L2**, and **L3** in dilute chloroform solutions and as thin films were investigated, and spectra are shown in Fig. 1. In solution form, **L1**, **L2**, and **L3** display a broad absorption band, with the maximum absorption peaks located at 697, 724, and 738 nm, respectively. It can be found that the absorption peak is obviously redshifted upon increasing the conjugation length. The asymmetric acceptor **L2** exhibits the largest molar absorption coefficient (1.7×10^5 M^{-1} cm^{-1}) among these three acceptors (**L1**: 1.56×10^5 M^{-1} cm^{-1}; and **L3**: 1.56×10^5 M^{-1} cm^{-1}). In going from solution to thin film, the absorption spectra of these acceptors are all redshifted, with two clear absorption peaks, indicating strong aggregation in the solid state. The maximum absorption peaks of **L1**, **L2**, and **L3** in thin-film form are located at 746, 776, and 814 nm, respectively. The optical bandgaps (E_g^{opt}) of **L1**, **L2**, and **L3** are calculated to be 1.49, 1.45, and 1.42 eV from the onset of film absorption based on the equation: $E_g^{opt} = 1240/\lambda_{edge}$. Cyclic voltammetry (CV) measurements were used to estimate the energy levels of the acceptors. The highest occupied molecular orbital (HOMO) and lowest unoccupied molecular orbital (LUMO) energy levels can be calculated based on the equation: $E_{HOMO/LUMO} = -e(E_{ox/red} - E_{(Fc/Fc+)} + 4.8)$ (eV). As shown in Fig. 2, the HOMO/LUMO energy levels were determined to be −5.68/−3.79 eV for **L1**, −5.56/−3.88 eV for **L2**, and −5.38/−3.87 eV for **L3**. The introduction of π-bridge units can significantly lift the HOMO energy levels due to electron-donating features. In addition, the detailed electrochemical and optical properties are summarized in Table 1.

The molecular geometries and energy levels of these three acceptors were investigated based on density functional theory (DFT) calculations at the B3LYP/6-31G(d) level. The alkyl and alkoxyl side chains were simplified to methyl and methoxy to reduce the complexity of calculations. The calculated molecular conformations, HOMO/LUMO wave function distributions, and energy levels are shown in the ESI.† These three acceptors all display planar molecular geometries, which is beneficial for electron delocalization. The electron clouds of the HOMOs and LUMOs are uniformly distributed along the molecular backbones of the acceptors. The theoretical LUMO/HOMO energy levels are determined to be −3.93/−6.06 eV for **L1**, −3.77/−5.81 eV for **L2**, and −3.62/−5.63 eV for **L3**, which is consistent with the CV measurements.

The photovoltaic performances of **L1**, **L2**, and **L3** can be evaluated using inverted devices with an ITO/ZnO/polymer: acceptor/MoO_3/Ag configuration, where commonly used PBDB-T was chosen as the donor polymer due to its complementary absorption and matched energy levels with these acceptors. The ZnO layer was prepared according to a procedure in the literature.[35] The synthesis conditions, such as the polymer concentration, active layer composition, spin-coating rate, and additive, are systematically optimized. The detailed optimization process is described in the ESI.† As shown in Fig. 3 and Table 2, the device based on the asymmetric acceptor **L2** exhibits the highest PCE of 14.06%, with an open-circuit voltage (V_{oc},) of 0.82 V, a short-circuit current (J_{sc}) of 24.01 mA cm^{-2}, and a fill factor (FF) of 71.73%, which is much higher than the PCEs of OSCs based on the symmetric acceptors **L1** (2.07%) and **L3** (1.78%). It is obvious that small structural variations in the acceptor molecules caused huge differences in device performance. The main reason for the very low power conversion efficiency of the device based on **L1** is probably its extremely low charge mobility, whereas the low efficiency of the device based on **L3** is probably caused by its poor blend film morphology (*vide infra*). With an increase in the conjugation length, the V_{oc} values of the devices increased from 0.69 V for **L1** to 0.82 V

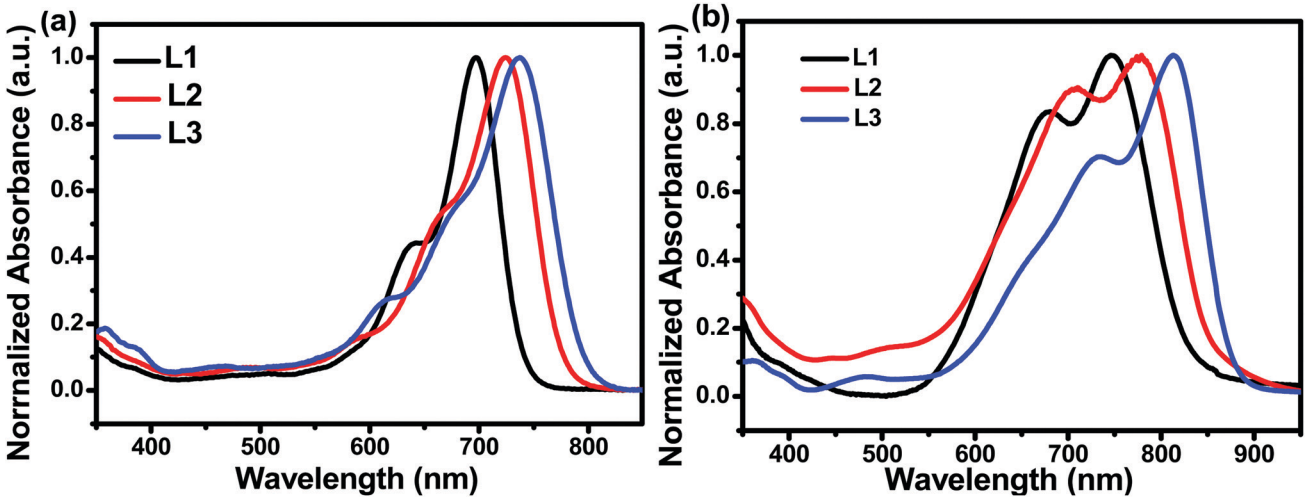

Fig. 1 UV-Vis absorption spectra of **L1**, **L2**, and **L3** in $CHCl_3$ solutions (a) and as thin films (b).

 This journal is © The Royal Society of Chemistry 2022

Published on 17 novembra 2021. Downloaded on 13.10.2025 2:24:29.

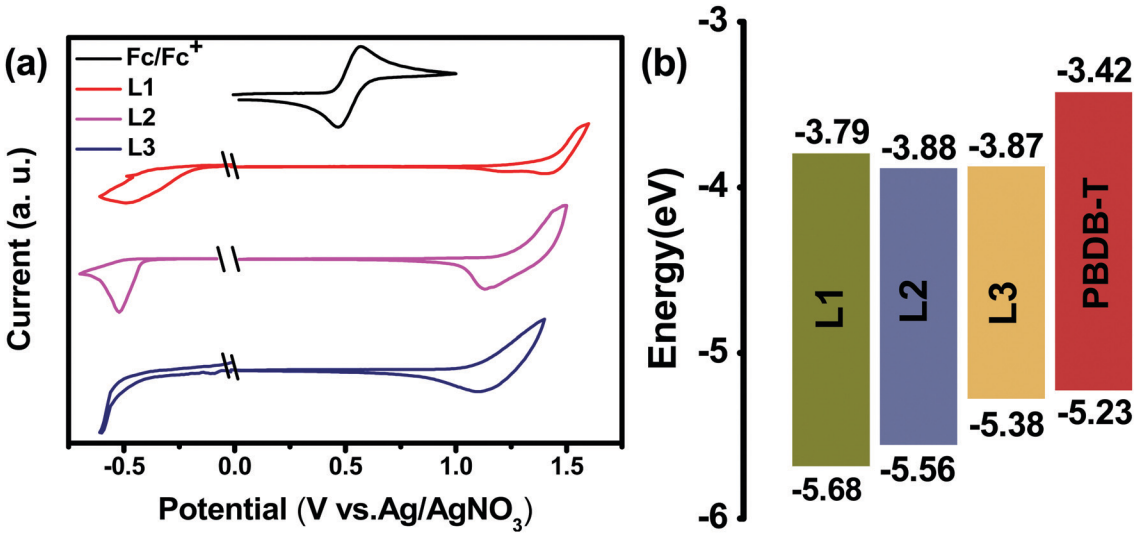

Fig. 2 (a) The electrochemical properties of **L1**, **L2**, and **L3** from cyclic voltammetry. (b) An energy band diagram showing the acceptor and donor HOMO/LUMO positions.

Table 1 The optical and electrochemical properties of **L1**, **L2**, and **L3**

Acceptor	$\lambda_{max}{}^{a}$ (nm)	$\lambda_{max}{}^{b}$ (nm)	E_g^{opt} (eV)	HOMO (eV)	LUMO (eV)
L1	697	746	1.49	−5.68	−3.79
L2	724	776	1.45	−5.56	−3.88
L3	738	814	1.42	−5.38	−3.87

[a] In dilute chloroform solution. [b] As thin film.

for **L2** to 0.91 V for **L3**. External quantum efficiency (EQE) measurements are used to verify the accuracy of the J_{sc} values obtained from *J*–*V* curves. As shown in Fig. 3, **L2**-based devices possess the best photo-to-current response among these three acceptors, and the maximum EQE value approaches approximately 80%, which is consistent with the *J*–*V* curve results. To reveal the reasons behind the huge device performance differences between these three acceptors, detailed characterization, including morphology, charge mobility, charge recombination behavior, and energy loss analysis, of the devices was carried out (*vide infra*). Moreover, the stability of the **L2**-based device arrangement is also measured. As shown in the ESI,† the PCE of an **L2**-based device maintains 86% of its initial value after being placed in a glove box for 168 h, which implies the good stability of the asymmetric acceptor.

A systematic investigation of the charge recombination behaviour can provide better understanding of the significant difference in FF values between OSCs based on **L1**, **L2**, and **L3**. The relationship between J_{sc} and light intensity (P_{light}) can be described as $J_{sc} \propto P_{light}{}^{\alpha}$, in which α is an exponential factor representing bimolecular recombination. As shown in Fig. 3, J_{sc} and P_{light} were plotted in a log–log plot. The α values of the **L1**- and **L3**-based devices are 0.91 and 0.83, respectively, much lower than that of a device based on **L2** (0.98). Typically speaking, a higher α value, especially approaching 1, means more efficient photogenerated exciton transport and much reduced geminate recombination loss, which is beneficial for achieving a higher FF.[36] Therefore, J_{sc} *vs.* P_{light} measurements can explain well why the **L2**-based device has the highest FF among these three acceptors. Further, the photocurrent density (J_{ph}) and effective voltage (V_{eff}) are also measured and used to reveal the charge recombination processes in the OSCs. Using the equation $J_{ph} = J_L - J_D$, J_{ph} can be calculated, where J_L and J_D represent the photocurrent densities under light and in the dark, respectively. Similarly, in the equation $V_{eff} = V_o - V$, V_o represents the voltage when $J_L = J_D$, and V is the applied voltage. As shown in Fig. 3, **L1**- and **L3**-based OSCs cannot achieve saturated photocurrent density (J_{sat}) even when V_{eff} approaches 1, indicating serious charge recombination in the devices. In comparison, **L2**-based devices reach J_{sat} with a J_{ph}/J_{sat} ratio of 0.94, indicating efficient exciton dissociation and suppressed charge recombination. All in all, these charge recombination behaviour investigations can reveal well the reasons for the much higher FF of **L2**-based devices than **L1**- and **L3**-based ones.

Energy loss (E_{loss}) analysis is conducted based on highly sensitive external quantum efficiency (sEQE) and electroluminescence (EL) measurements to understand the V_{oc} differences between OSCs based on these different acceptors. E_{loss} can be calculated based on the equation $E_{loss} = E_g - qV_{oc}$, where E_g is the corresponding cross-point of UV-vis and photoluminescence (PL) spectra.[37] As shown in Table 3, **L1**-, **L2**-, and **L3**-based devices display E_{loss} values of 0.85, 0.68, and 0.55 eV, respectively. As shown in Fig. 4, the charge transfer state energy (E_{ct}) of the blend films can be estimated based on the cross-point of Gaussian fitting curves of the sEQE and EL curves. Accordingly, the E_{ct} values of **L1**-, **L2**-, and **L3**-based devices are 1.29, 1.36, and 1.39 eV, respectively. The tendencies of the E_{loss} and E_{ct} variations can explain the V_{oc} trend; that is, the higher E_{ct} and lower E_{loss} values of the **L3**-based device result in it showing the highest V_{oc} value among the devices based on these three acceptors. Furthermore, the energy loss of

Published on 17 novembra 2021. Downloaded on 13.10.2025 2:24:29.

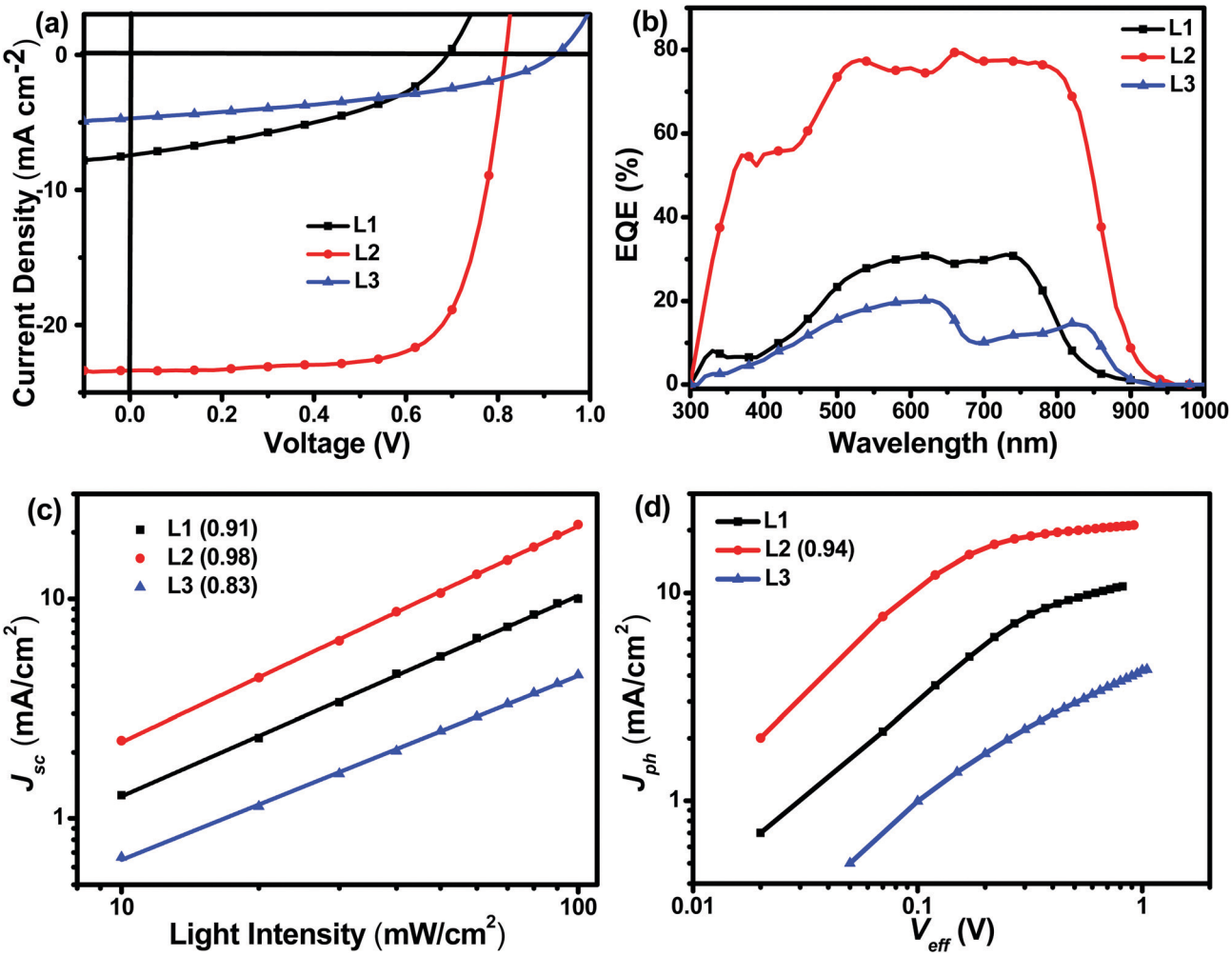

Fig. 3 (a) J–V and (b) EQE curves of **L1**-, **L2**-, and **L3**-based devices, (c) the dependence of J_{sc} on P_{light}, and (d) the dependence of J_{ph} on V_{eff}.

Table 2 The photovoltaic parameters of devices based on **L1**, **L2**, and **L3**

Acceptor	V_{oc} (V)	J_{SC} (mA cm^{-2})	FF (%)	$PCE_{max/ave}$ (%)
L1	0.69	7.44 (7.01)[a]	40.27	2.07 (1.99)[b]
L2	0.82	24.01 (22.74)[a]	71.73	14.06 (13.74)[b]
L3	0.91	4.70 (4.47)[a]	40.86	1.78 (1.67)[b]

[a] Integrated from EQE curves. [b] Average PCE from 5 devices.

OSCs can be divided into three parts: radiative energy loss (ΔE_1), charge generation energy loss (ΔE_2), and nonradiative energy loss (ΔE_3).[38–40] The ΔE_2 values, the difference between E_g and E_{ct}, of **L1**-, **L2**-, and **L3**-based devices are 0.25, 0.13, and 0.08 eV. ΔE_3 can be determined according to the equation $\Delta E_3 = k_B T/q \ln(1/EQE_{EL})$, where k_B, T, and q represent the Boltzmann constant, temperature, and elementary charge, respectively. The ΔE_3 values of **L1**-, **L2**-, and **L3**-based devices are 0.32, 0.27, and 0.20 eV, respectively. Finally, the ΔE_1 values, defined *via* removing ΔE_2 and ΔE_3 from E_{loss}, of **L1**-, **L2**-, and **L3**-based devices are 0.28, 0.28, and 0.27 eV, respectively. Above all, the asymmetric **L2**-based device displays medium energy loss. Our results demonstrate that asymmetric molecular design can achieve a balance between energy loss and photovoltaic performance.

The blend film morphologies are investigated *via* atomic force microscopy (AFM) and transmission electron microscopy (TEM) to understand the photovoltaic performances of the OSCs based on these acceptors. As shown in Fig. 5, AFM images of blend films based on PBDB-T:**L1** and PBDB-T:**L2** show homogeneous surface morphologies without apparent large-scale

Table 3 Parameters measured or calculated using EL and sEQE

Active layer	E_g [eV]	E_{ct} [eV]	EQE_EL [%]	E_{loss} [eV]	ΔE_1 [eV]	ΔE_2 [eV]	ΔE_3 [eV]
PBDB-T:**L1**	1.54	1.29	1.13×10^{-4}	0.85	0.28	0.25	0.32
PBDB-T:**L2**	1.49	1.36	6.99×10^{-4}	0.68	0.28	0.13	0.27
PBDB-T:**L3**	1.47	1.39	2.61×10^{-2}	0.55	0.27	0.08	0.20

 This journal is © The Royal Society of Chemistry 2022

Published on 17 novembra 2021. Downloaded on 13.10.2025 2:24:29.

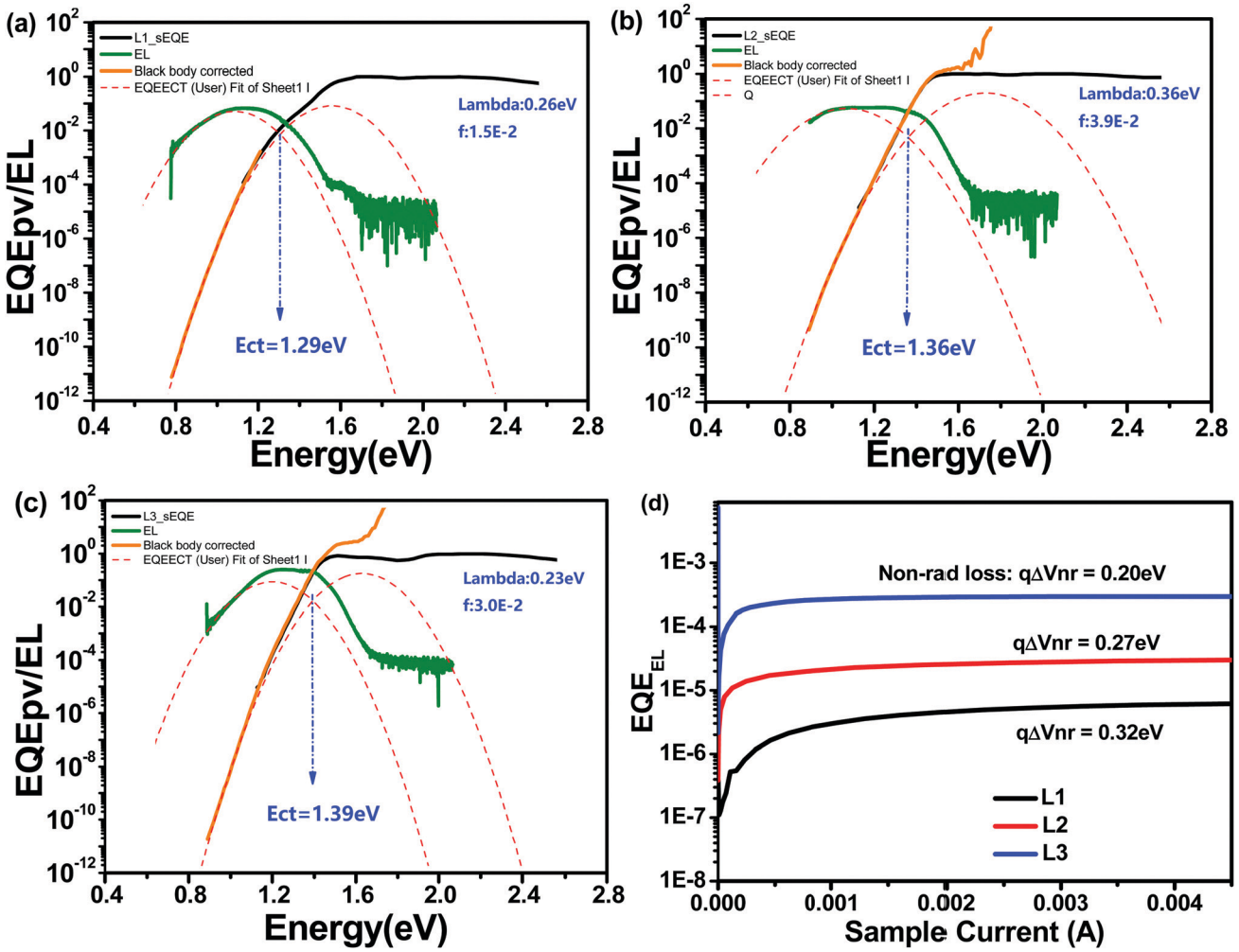

Fig. 4 Normalized sEQE spectra of solar cells based on **L1** (a), **L2** (b), and **L3** (c), and EL curves (d).

phase separation, while the blend film based on PBDB-T:**L3** shows large-scale phase separation. The root-mean-square (RMS) roughness values of 2.11 nm for PBDB-T:**L1**, 1.48 nm for PBDB-T:**L2**, and 5.65 nm for PBDB-T:**L3** are obtained from AFM height images. Obviously, **L2**-based blend film has a more homogenous phase morphology, with the lowest RMS value. In addition, the TEM results are consistent with the AFM measurements. PBDB-T:**L3** blend film displays apparent larger-scale phase separation, with large dark and light regions, which are more obvious in the inset of Fig. 5f. As for PBDB-T:**L1** blend film, moderate phase separation morphology is seen, with sparse and burly fibrils. PBDB-T:**L2** blend film exhibits appropriate phase separation, with fibrils having diameters of 10 to 20 nm, which is beneficial for charge transport, thus leading to the high J_{sc} and FF values of related OSCs. We speculate that the reason for the formation of different morphologies is the varied solubilities of acceptors. More specifically speaking, the asymmetric acceptor **L2** possesses the best solubility among these acceptors (*vide supra*), which can delay precipitation during the film-deposition process, thus, better film morphology can be formed.[41] To investigate the charge-transport properties of the

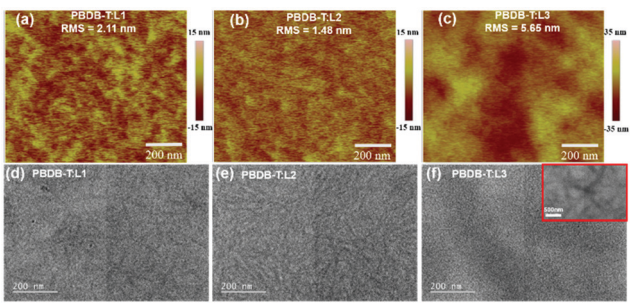

Fig. 5 AFM and TEM images of PBDB-T:**L1** film (a and d), PBDB-T:**L2** film (b and e), and PBDB-T:**L3** film (c and f).

devices, the space-charge limited current (SCLC) method was utilized to estimate the hole (μ_h) and electron (μ_e) transport mobilities based on typical device configurations of ITO/PEDOT:PSS/active layer/Au and ITO/ZnO/active layer/Al, respectively. As shown in the ESI,† PBDB-T:**L1** blend film displays inferior μ_h and μ_e values of 7.57×10^{-6} cm^2 V^{-1} s^{-1} and 1.47×10^{-6} cm^2 V^{-1} s^{-1}, respectively. For PBDB-T:**L3** blend film, the μ_h and μ_e values are

Published on 17 novembra 2021. Downloaded on 13.10.2025 2:24:29.

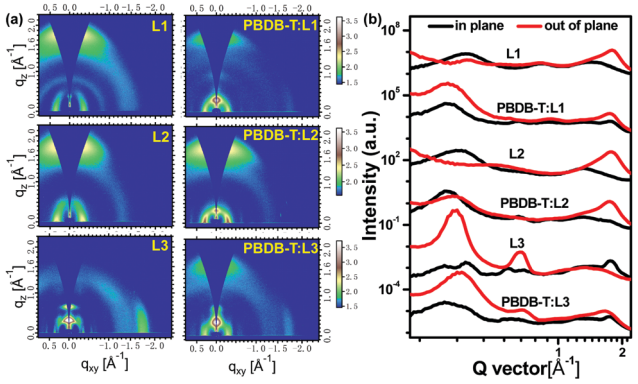

Fig. 6 (a) 2D GIWAXS patterns and (b) 1D scattering profiles of neat **L1**, **L2**, and **L3** films and corresponding blend films.

slightly higher, with values of 3.49×10^{-5} cm^2 V^{-1} s^{-1} and 3.28×10^{-6} cm^2 V^{-1} s^{-1}, respectively. More impressively, PBDB-T:**L2** blend film possesses the highest μ_h and μ_e values of 1.52×10^{-4} cm^2 V^{-1} s^{-1} and 1.48×10^{-4} cm^2 V^{-1} s^{-1}, with a μ_h/μ_e ratio of 1.03. The significantly higher and more balanced hole and electron transport mobilities of the **L2**-based device can explain its superior J_{sc} and FF values, which lead to the observably higher photovoltaic performance out of these three acceptors.

Grazing-incidence wide-angle X-ray scattering (GIWAXS) measurements are used to investigate molecular orientation and packing. As shown in Fig. 6, neat **L1** and **L2** films display an obvious (010) diffraction peak in the out-of-plane (OOP) direction and a (100) diffraction peak in the in-plane (IP) direction, indicating the formation of a predominantly face-on orientation. In particular, neat **L2** film exhibits much stronger (010) diffraction, based on the 2D GIWAXS pattern and 1D profile, indicating the high crystallinity of **L2**. Conversely, a dominant edge-on molecular orientation is formed in neat **L3** film, with observable (010) and (100) diffraction peaks in the IP and OOP directions, respectively. The π–π stacking distances of **L1**, **L2**, and **L3** are quite similar, all about 3.50 Å. The lamellar stacking distance is gradually increased from **L1** (17.44 Å) to **L2** (18.48 Å) to **L3** (19.63 Å), probably reflecting the molecular backbone lengths of the acceptors. Both **L1** and **L2** in blend films with PBDB-T adopt preferential face-on orientations. Also, the (010) diffraction of **L2**-based blend film is much stronger than that of the **L1**-based example. However, PBDB-T:**L3** blend film displays mixed molecular orientations (face-on and edge-on) based on the 2D GIWAXS pattern and 1D profile. In addition, the crystal coherence length (CCL) is estimated to analyse the crystallinity quality.[42,43] Based on the equation CCL = 2π/FWHM, the CCL values of the (010) diffraction peaks in the OOP direction were 21.83, 22.09, and 16.34 Å for PBDB-T:**L1**, PBDB-T:**L2**, and PBDB-T:**L3** films, respectively, indicating that **L2**-based blend film has the best crystallinity quality.[44] All in all, molecular orientation and stacking analysis can explain well the excellent photovoltaic performance of the **L2**-based device.

Conclusions

In summary, three low-bandgap non-fullerene acceptors (**L1**, **L2**, and **L3**) are designed and synthesized *via* regulating the π-bridge units. Assisted by a symmetry-breaking strategy, the asymmetric acceptor **L2**, with one π-bridge thiophene unit, displays the best solubility among these three acceptors, which helps form appropriate phase morphology. In addition, **L2** possesses a higher molar absorption coefficient in solution. In particular, asymmetric **L2** and its corresponding blend film exhibit a predominantly face-on orientation and strong crystallinity, which can facilitate charge transport. As expected, much higher and more balanced hole and electron mobilities are achieved in **L2**-based devices. Hence, a high PCE of 14.06% is achieved in a device based on the asymmetric acceptor **L2**, which is much higher than those obtained using its symmetric counterparts (2.17% for **L1** and 1.78% for **L3**). Device physics investigations reveal that **L2**-based devices exhibit low charge recombination and moderate energy loss. All in all, our work provides an effective way to fabricate high-performance non-fullerene acceptors *via* a symmetry-breaking strategy.

Conflicts of interest

There are no conflicts to declare.

Acknowledgements

The authors gratefully acknowledge financial support from the National Natural Science Foundation of China (51933001) and China Postdoctoral Science Foundation (2018M641033).

Notes and references

1 A. Armin, W. Li, O. J. Sandberg, Z. Xiao, L. Ding, J. Nelson, D. Neher, K. Vandewal, S. Shoaee, T. Wang, H. Ade, T. Heumüller, C. Brabec and P. Meredith, *Adv. Energy Mater.*, 2021, **11**, 20003570.
2 K. Sreedhar Ram, H. Mehdizadeh-Rad, D. Ompong, D. D. Y. Setsoafia and J. Singh, *Nanomaterials*, 2021, **11**, 209.
3 Y. Un Kim, G. Eun Park, S. Choi, D. Hee Lee, M. Ju Cho and D. H. Choi, *J. Mater. Chem. C*, 2017, **5**, 7182–7190.
4 R. Li, G. Liu, R. Xie, Z. Wang, X. Yang, K. An, W. Zhong, X.-F. Jiang, L. Ying, F. Huang and Y. Cao, *J. Mater. Chem. C*, 2018, **6**, 7046–7053.
5 Y. Cui, H. Yao, L. Hong, T. Zhang, Y. Tang, B. Lin, K. Xian, B. Gao, C. An, P. Bi, W. Ma and J. Hou, *Natl. Sci. Rev.*, 2020, **7**, 1239–1246.
6 L. Huo, T. Liu, B. Fan, Z. Zhao, X. Sun, D. Wei, M. Yu, Y. Liu and Y. Sun, *Adv. Mater.*, 2015, **27**, 6969–6975.
7 Q. Liu, Y. Jiang, K. Jin, J. Qin, J. Xu, W. Li, J. Xiong, J. Liu, Z. Xiao, K. Sun, S. Yang, X. Zhang and L. Ding, *Sci. Bull.*, 2020, **65**, 272–275.
8 Y. Cui, Y. Xu, H. Yao, P. Bi, L. Hong, J. Zhang, Y. Zu, T. Zhang, J. Qin, J. Ren, Z. Chen, C. He, X. Hao, Z. Wei and J. Hou, *Adv. Mater.*, 2021, **33**, 2102420.
9 Z. Liu, X. Zhang, P. Li and X. Gao, *Sol. Energy*, 2018, **174**, 171–188.

 This journal is © The Royal Society of Chemistry 2022

Published on 17 novembra 2021. Downloaded on 13.10.2025 2:24:29.

10 J. Miao, B. Meng, J. Liu and L. Wang, *Chem. Commun.*, 2018, **54**, 303–306.
11 K. Jin, C. Deng, L. Zhang, D. Li, T. Li, F. Wang, Y. Yuan, Z. Xiao and L. Ding, *Mater. Chem. Front.*, 2018, **2**, 1716–1719.
12 Y.-N. Chen, R. Zheng, J. Wang, H. Wang, M. Li, Y. Wang, H. Lu, Z. Zhang, Y. Liu, Z. Tang and Z. Bo, *J. Mater. Chem. C*, 2021, **9**, 6937–6943.
13 Y. Liu, C. e. Zhang, D. Hao, Z. Zhang, L. Wu, M. Li, S. Feng, X. Xu, F. Liu, X. Chen and Z. Bo, *Chem. Mater.*, 2018, **30**, 4307–4312.
14 C. He, Y. Li, Y. Liu, Y. Li, G. Zhou, S. Li, H. Zhu, X. Lu, F. Zhang, C.-Z. Li and H. Chen, *J. Mater. Chem. A*, 2020, **8**, 18154–18161.
15 H. Yao, Y. Cui, R. Yu, B. Gao, H. Zhang and J. Hou, *Angew. Chem., Int. Ed.*, 2017, **56**, 3045–3049.
16 J. Yuan, Y. Zhang, L. Zhou, G. Zhang, H.-L. Yip, T.-K. Lau, X. Lu, C. Zhu, H. Peng, P. A. Johnson, M. Leclerc, Y. Cao, J. Ulanski, Y. Li and Y. Zou, *Joule*, 2019, **3**, 1140–1151.
17 S. Pang, X. Zhou, S. Zhang, H. Tang, S. Dhakal, X. Gu, C. Duan, F. Huang and Y. Cao, *ACS Appl. Mater. Interfaces*, 2020, **12**, 16531–16540.
18 H. Yu, Z. Qi, X. Li, Z. Wang, W. Zhou, H. Ade, H. Yan and K. Chen, *Sol. RRL*, 2020, **4**, 200421.
19 X. Liu, Y. Wei, X. Zhang, L. Qin, Z. Wei and H. Huang, *Sci. China: Chem.*, 2020, **64**, 228–231.
20 G. Chai, Y. Chang, J. Zhang, X. Xu, L. Yu, X. Zou, X. Li, Y. Chen, S. Luo, B. Liu, F. Bai, Z. Luo, H. Yu, J. Liang, T. Liu, K. S. Wong, H. Zhou, Q. Peng and H. Yan, *Energy Environ. Sci.*, 2021, **6**, 3469–3479.
21 S. Feng, C. Zhang, Y. Liu, Z. Bi, Z. Zhang, X. Xu, W. Ma and Z. Bo, *Adv. Mater.*, 2017, **29**, 1703527.
22 J. Yang, Q. Li and Z. Li, *Phys. Chem. Chem. Phys.*, 2021, **23**, 12321–12328.
23 C. Li, J. Song, L. Ye, C. Koh, K. Weng, H. Fu, Y. Cai, Y. Xie, D. Wei, H. Y. Woo and Y. Sun, *Sol. RRL*, 2019, **3**, 1800246.
24 J. Song, C. Li, L. Ye, C. Koh, Y. Cai, D. Wei, H. Y. Woo and Y. Sun, *J. Mater. Chem. A*, 2018, **6**, 18847–18852.
25 Z. Luo, G. Li, K. Wu, Z.-G. Zhang, X. Chen, B. Qiu, L. Xue, Y. Li and C. Yang, *Org. Electron.*, 2018, **62**, 82–88.
26 Y. Yin, J. Song, F. Guo, Y. Sun, L. Zhao and Y. Zhang, *ACS Appl. Energy Mater.*, 2018, **1**, 6577–6585.
27 C. Li, Y. Xie, B. Fan, G. Han, Y. Yi and Y. Sun, *J. Mater. Chem. C*, 2018, **6**, 4873–4877.
28 F. Chen, G. Ding, A. Tang, B. Xiao, J. Li and E. Zhou, *J. Mater. Chem. C*, 2018, **6**, 2580–2587.
29 W. Gao, H. Fu, Y. Li, F. Lin, R. Sun, Z. Wu, X. Wu, C. Zhong, J. Min, J. Luo, H. Y. Woo, Z. Zhu and A. K. Y. Jen, *Adv. Energy Mater.*, 2020, **11**, 2003177.
30 Y. Chen, F. Bai, Z. Peng, L. Zhu, J. Zhang, X. Zou, Y. Qin, H. K. Kim, J. Yuan, L. K. Ma, J. Zhang, H. Yu, P. C. Y. Chow, F. Huang, Y. Zou, H. Ade, F. Liu and H. Yan, *Adv. Energy Mater.*, 2020, **11**, 2003141.
31 S. Li, L. Zhan, N. Yao, X. Xia, Z. Chen, W. Yang, C. He, L. Zuo, M. Shi, H. Zhu, X. Lu, F. Zhang and H. Chen, *Nat. Commun.*, 2021, **12**, 4627.
32 Q. Guo, J. Lin, H. Liu, X. Dong, X. Guo, L. Ye, Z. Ma, Z. Tang, H. Ade, M. Zhang and Y. Li, *Nano Energy*, 2020, **74**, 104861.
33 B. Fan, D. Zhang, M. Li, W. Zhong, Z. Zeng, L. Ying, F. Huang and Y. Cao, *Sci. China: Chem.*, 2019, **62**, 746–752.
34 X. Ji, T. Zhou, X. Ke, W. Wang, S. Wu, M. Zhang, D. Lu, X. Zhang and Y. Liu, *J. Mater. Chem. C*, 2020, **8**, 5163–5170.
35 Y. Sun, J. H. Seo, C. J. Takacs, J. Seifter and A. J. Heeger, *Adv. Mater.*, 2011, **23**, 1679–1683.
36 M. Lenes, M. Morana, C. J. Brabec and P. W. M. Blom, *Adv. Funct. Mater.*, 2009, **19**, 1106–1111.
37 R. Yu, H. Yao, Y. Cui, L. Hong, C. He and J. Hou, *Adv. Mater.*, 2019, **31**, 1902302.
38 Z. Zhou, S. Xu, J. Song, Y. Jin, Q. Yue, Y. Qian, F. Liu, F. Zhang and X. Zhu, *Nat. Energy*, 2018, **3**, 952–959.
39 J. Yao, T. Kirchartz, M. S. Vezie, M. A. Faist, W. Gong, Z. He, H. Wu, J. Troughton, T. Watson, D. Bryant and J. Nelson, *Phys. Rev. Appl.*, 2015, **4**, 014020.
40 S. M. Menke, N. A. Ran, G. C. Bazan and R. H. Friend, *Joule*, 2018, **2**, 25–35.
41 J. J. Franeker, H. L. Heintges, C. Schaefer, G. Portale, W. Li, M. M. Wienk, P. Schoot and A. J. Janssen, *J. Am. Chem. Soc.*, 2015, **137**, 11783–11794.
42 L. Yang, S. Zhang, C. He, J. Zhang, Y. Yang, J. Zhu, Y. Cui, W. Zhao, H. Zhang, Y. Zhang, Z. Wei and J. Hou, *Chem. Mater.*, 2018, **30**, 2129–2134.
43 Y. Yang, Z. G. Zhang, H. Bin, S. Chen, L. Gao, L. Xue, C. Yang and Y. Li, *J. Am. Chem. Soc.*, 2016, **138**, 15011–15018.
44 T. J. Aldrich, S. M. Swick, F. S. Melkonyan and T. J. Marks, *Chem. Mater.*, 2017, **29**, 10294–10298.